Lithium Diffusion in Niobium Tungsten Oxide Shear Structures

Can P. Koçer,[1,*] Kent J. Griffith,[2,3] Clare P. Grey,[3] and Andrew J. Morris[4]

[1] *Theory of Condensed Matter, Cavendish Laboratory, University of Cambridge, J. J. Thomson Avenue, Cambridge CB3 0HE, UK*
[2] *Department of Materials Science and Engineering, Northwestern University, Evanston, Illinois, 60208, USA*
[3] *Department of Chemistry, University of Cambridge, Lensfield Road, Cambridge CB2 1EW, UK*
[4] *School of Metallurgy and Materials, University of Birmingham, Edgbaston, Birmingham B15 2TT, UK*

(Dated: April 20, 2020)

Niobium tungsten oxides with crystallographic shear structures form a promising class of high-rate Li-ion anode materials. Lithium diffusion within these materials is studied in this work using density-functional theory calculations, specifically nudged elastic band (NEB) calculations and *ab initio* molecular dynamics (AIMD) simulations. Lithium diffusion is found to occur through jumps between fourfold coordinated window sites with low activation barriers (80–300 meV), and is constrained to be effectively one-dimensional by the crystallographic shear planes of the structures. We identify a number of other processes, including rattling motions with barriers on the order of the thermal energy at room temperature, and intermediate barrier hops between fourfold and fivefold coordinated lithium sites. We demonstrate differences regarding diffusion pathways between different cavity types; within the ReO_3-like block units of the structures, cavities at the corners and edges host more isolated diffusion tunnels than those in the interior. Diffusion coefficients are found to be in the range of 10^{-12}–10^{-11} m^2s^{-1} for lithium concentrations of 0.5 Li/TM. Overall, the results provide a complete picture of the diffusion mechanism in niobium tungsten oxide shear structures, and the structure–property relationships identified in this work can be generalised to the entire family of crystallographic shear phases.

I. INTRODUCTION

Li-ion batteries with short charge times and high power density are required to accelerate consumer adoption of electric vehicles and relieve intermittency of renewable energy resources [1, 2]. While there are many factors determining the charge/discharge rate of a device [1], and not all materials with high-rate capability are suited for each application, the ionic and electronic conduction within the active materials represent fundamental limits to the achievable rate. Lithium diffusion in electrode materials, quantified by a diffusion coefficient D, is usually much slower than in the electrolyte (liquid or solid). To achieve high rates, the slower diffusion can be compensated by nanostructuring the electrode material, decreasing the diffusion length L, and thereby reducing the time $\tau = L^2/D$ required to lithiate a particle. However, nanostructuring, as commonly applied to $Li_4Ti_5O_{12}$ and TiO_2, has disadvantages in terms of cost and stability, and can be avoided if the electrode material has intrinsically fast lithium diffusion.

A number of niobium-based complex oxides with open framework structures show very fast lithium diffusion, and are promising for applications as high-rate, high-voltage anodes. These include T-Nb_2O_5 [4], $TiNb_2O_7$ [5], and the recently discovered niobium tungsten oxides $Nb_{16}W_5O_{55}$ and $Nb_{18}W_{16}O_{93}$ [6], among others. The present work focuses on niobium tungsten oxides with Wadsley–Roth crystallographic shear structures, specifically $Nb_{12}WO_{33}$, $Nb_{14}W_3O_{44}$, $Nb_{16}W_5O_{55}$, and $Nb_{18}W_8O_{69}$. These materials feature crystal structures comprised of ReO_3-like blocks of $n \times m$ corner-sharing

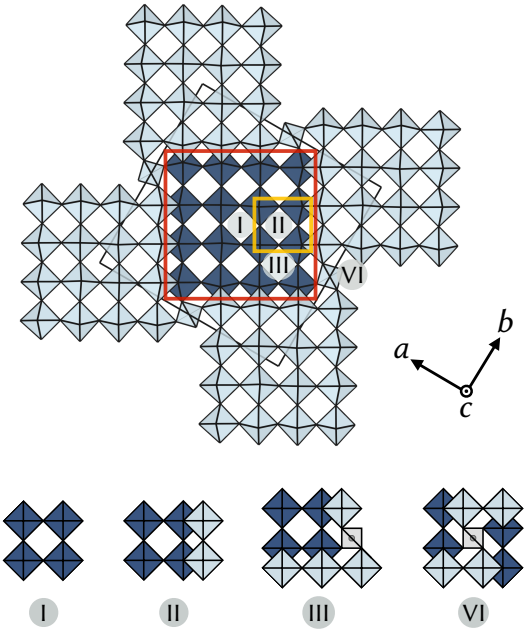

FIG. 1. Crystal structure of $Nb_{14}W_3O_{44}$ (space group $I4/m$). Light and dark blocks are offset by $\frac{1}{2}c$. The 4×4 block is framed by crystallographic shear planes (edges of red square). Four types of cavities (Cava classification [3], bottom, view along c) occur in $Nb_{14}W_3O_{44}$, and a single type II cavity is framed by the yellow square.

* cpk27@cam.ac.uk

octahedra (light and dark blue in Fig. 1). Blocks are connected to each other along crystallographic shear planes (Fig. 1, red square), and tetrahedral sites are present at the corners of the blocks to fill voids. Along the direction perpendicular to the plane of the block, the blocks connect to form columns (c direction in Fig. 1). The niobium tungsten oxides differ in the size of the blocks; $Nb_{12}WO_{33}$ features blocks of size 3×4, $Nb_{14}W_3O_{44}$ size 4×4 (Fig. 1), $Nb_{16}W_5O_{55}$ size 4 × 5, and $Nb_{18}W_8O_{69}$ size 5 × 5. The blocks feature different types of cavities/tunnels (Fig. 1), first categorised by Cava et al. [3]. Niobium tungsten oxide shear structures feature cavities of types I, II, III and VI, except for $Nb_{12}WO_{33}$ which does not contain a type I cavity due to its smaller block size. Cavities of type IV and V are present in other shear structures (e.g. $TiNb_2O_7$), but not in the materials studied here. The type VI cavity is special because, in comparison to the others, the open space within it is blocked by the tetrahedral site.

Lithium intercalation into niobium tungsten oxides has been studied both experimentally [6–10] and computationally [11]. Recent mechanistic studies have highlighted the role of local and long-range structural changes during lithium insertion. Experimental [12] and computational [11, 13] studies on shear structures observe good electronic conductivity, suggesting that electronic conduction is not rate-limiting. Lithium diffusion in $Nb_{16}W_5O_{55}$ has been studied by pulsed-field-gradient NMR spectroscopy, observing large diffusion coefficients of 10^{-12}–10^{-13} m^2s^{-1} at room temperature, and low activation energies of 0.1–0.2 eV [6]. Diffusivities for $Nb_{18}W_8O_{69}$, measured using the same technique, are slightly larger [14]. Measurements of diffusion coefficients and activation energies for lithium diffusion in $Nb_{12}WO_{33}$ and $Nb_{14}W_3O_{44}$ are currently not available but are expected to be in the same range. Regarding the mechanism, bond valence sum maps [6, 14] and computational results for structurally similar compounds (e.g. $TiNb_2O_7$, Ref. [15]) suggest one-dimensional diffusion down the block tunnels.

In this article, we study lithium diffusion within niobium tungsten oxide shear structures $Nb_{12}WO_{33}$ and $Nb_{14}W_3O_{44}$ using first-principles density-functional theory calculations. Building on our previous computational work on the lithium insertion mechanism of these materials [11], the aim of the present study is to understand the lithium diffusion mechanism of niobium tungsten oxides. In keeping with the approach from that study, structures with smaller block sizes are studied explicitly, and the results are extrapolated to the whole family. Due to their use as electrode materials, the lithium concentration in the niobium tungsten oxides varies as the battery operates, and this requires an analysis of the diffusion as a function of lithium concentration. To piece together the diffusion mechanism of niobium tungsten oxide shear structures over a range of lithium concentrations, we use two different methods: nudged elastic band (NEB) calculations, and *ab initio* molecular dynamics (AIMD) simulations.

Nudged elastic band calculations [16] are used to find minimum energy paths over the potential energy surface connecting local minima of lithium sites, and to provide the activation energy for hopping between them. Activation energies can be related to hopping rates via transition state theory. NEB calculations are computationally more efficient than AIMD simulations and provide insight into lithium diffusion at low lithium concentrations. At higher lithium concentrations, the dependence of the activation energy on the local lithium arrangement becomes important. For the niobium tungsten oxides, the complexity of the crystal structures and the structural changes during lithium intercalation make it cumbersome to probe all barriers at all states of charge, so another method is required. AIMD simulations probe the lithium dynamics at a given temperature directly, and take into account both temperature effects and Li–Li interactions. Diffusion coefficients and lithium probability distributions at any concentration can be determined, and AIMD simulations are thus the method of choice for higher lithium concentrations.

The article is structured as follows. We begin by studying lithium diffusion in the dilute limit in $Nb_{12}WO_{33}$ and $Nb_{14}W_3O_{44}$ using NEB calculations, establishing activation barriers, diffusion dimensionality, and the impact of structural features on diffusion. AIMD simulation results are presented next, providing a clear picture of diffusion pathways and estimates of diffusivities. We discuss how these results extrapolate to the other niobium tungsten oxide structures and how they relate to experimental measurements. We conclude by suggesting directions for future work.

II. METHODS

DFT calculations were performed with the VASP code [17], using projector augmented-wave potentials [18] to describe the interaction between core and valence electrons. The following atomic states were treated as valence: Li 1s and 2s, O 2s and 2p, Nb 4s, 4p, 4d, 5s, and 5p, W 5s, 5p, 5d, 6s, and 6p. The PBEsol [19] functional was used for all calculations. Previous work has demonstrated that magnetism and electron localisation in n-doped crystallographic shear phases is weak, and that the materials quickly become metallic or very good semiconductors during lithium intercalation [11–13, 15]. All calculations were therefore performed without spin-polarisation or Hubbard U corrections for the transition metal d-orbitals.

Structure models for $Nb_{12}WO_{33}$ and $Nb_{14}W_3O_{44}$ were obtained from a previous study [11]. For each structure, the lowest energy cation configuration was used. Lattice parameters and atomic positions of $Nb_{12}WO_{33}$ and $Nb_{14}W_3O_{44}$ were optimised using a planewave kinetic energy cutoff of 700 eV and a **k**-point grid spacing of 0.2 $Å^{-1}$, until the force on each atom was smaller than

0.01 eV/Å. Input structures for AIMD simulations were optimised using the same parameters. In the case of input structures for NEB calculations, only the atomic positions were optimised to keep the cell fixed during the transition state search.

Nudged Elastic Band Calculations. Nudged elastic band [16] calculations were performed in supercells of $Nb_{12}WO_{33}$ and $Nb_{14}W_3O_{44}$, containing 92 and 122 non-Li atoms, respectively. The supercell construction is described in more detail in the Supporting Information. All NEB calculations were performed using the VTST tools code plugin, with a planewave kinetic energy cutoff of 700 eV and a **k**-point grid spacing of 0.2 $Å^{-1}$ to sample the Brillouin zone. Initial Li positions were obtained from our previous DFT study [11]. A single Li atom was inserted into the supercell at each position and the structure was optimised with a fixed lattice until the force on each atom was smaller than 0.01 eV/Å. Sites in close proximity were used as initial guesses for endpoints of minimum energy paths. Between 5–9 images were used to resolve the paths. In cases where an intermediate minimum was found between two endpoints, the intermediate was optimised and added as a new endpoint. The NEB calculations were stopped once the force on each image was smaller than 0.01 eV/Å. For very low-energy barriers ($E_a < 0.1$ eV), the convergence of the barrier value was verified with a smaller force tolerance of 0.005 eV/Å.

As the energies of the states before and after a lithium-ion hop may differ, kinetically-resolved activation barriers [20] ΔE_{KRA} are reported throughout:

$$\Delta E_{\mathrm{KRA}} = E_{\mathrm{TS}} - \frac{1}{2}(E_i + E_f) \tag{1}$$

where E_i and E_f are the energies of the initial and final states, and E_{TS} is the energy of the transition state (obtained from a spline interpolation of the energy profile). This removes the direction dependence of the activation barrier.

***Ab initio* molecular dynamics.** Structure models for lithiated phases were obtained from Ref. [11] and optimised (as described above). Supercells of $Li_xNb_{12}WO_{33}$ ($x = 5, 8, 17$) and $Li_8Nb_{14}W_3O_{44}$, containing 138 and 183 non-Li atoms, respectively, were constructed (see Supporting Information). To ensure a reasonable computational cost for the MD simulations, the planewave kinetic energy cutoff was reduced to 450 eV and **k**-point grids of $2 \times 2 \times 1$ and $2 \times 1 \times 1$ were used for the supercells of $Nb_{12}WO_{33}$ and $Nb_{14}W_3O_{44}$. The parameters were validated as described in the Supporting Information.

The MD simulations were performed in the NVT ensemble, using a Nosé–Hoover thermostat. The timestep was set to 1.5 fs. MD simulations were performed for temperatures of 600–1500 K, depending on the stoichiometry. The simulations have to be performed at elevated temperatures to be able to observe diffusion events within the system size and time constraints of AIMD simulations [21, 22]. The systems were heated to the final temperature over a period of 2 ps, with velocity scaling at each timestep. After an equilibration time of 6 ps, the simulations were run for at least 150 ps. Final configurations of AIMD runs were optimised and inspected to verify that the host framework had not changed. Simulations were performed for stoichiometries $Li_5Nb_{12}WO_{33}$, $Li_8Nb_{12}WO_{33}$, $Li_{17}Nb_{12}WO_{33}$, and $Li_8Nb_{14}W_3O_{44}$, but various problems were encountered during the AIMD simulations, and a detailed description is given in the Results section.

The tracer (or self-) diffusion coefficient D^* is defined as

$$D^* = \frac{1}{2d} \lim_{t\to\infty} \frac{d}{dt} \frac{1}{N} \sum_{i=1}^{N} \langle |\mathbf{r}_i(t+t_0) - \mathbf{r}_i(t_0)|^2 \rangle_{t_0} \tag{2}$$

$$= \frac{1}{2d} \lim_{t\to\infty} \frac{d}{dt} \langle \Delta\mathbf{r}^2(t) \rangle \tag{3}$$

where N is the number of diffusing particles, and d is the dimensionality of the diffusion ($d = 1$ for the Nb/W oxides, see below). We note that the averaging over initial times t_0 is essential to obtain well-converged results. The tracer diffusion coefficient was determined by a linear regression of $2dt$ against $\langle \Delta\mathbf{r}^2(t) \rangle$. Plots of the mean squared displacement as a function of time are available in the Supporting Information (Fig. S4). Assuming a temperature dependence of the diffusion coefficient of $D^*(T) = D_0\ e^{-\frac{E_a}{k_B T}}$, Arrhenius plots were constructed to determine the activation energy E_a. The diffusion coefficients at room temperature were obtained by extrapolating the Arrhenius expression, as AIMD simulations at room temperature are not feasible [21, 22].

The probability density distribution [23] of lithium ions in the structure, $P(\mathbf{r})$, was extracted from simulations at 900 K for all studied stoichiometries. $P(\mathbf{r})$ was obtained by counting the number of Li ions at each point on a uniform grid over the unit cell, and averaging over the simulation time. Resulting structures were visualised with VESTA [24].

III. RESULTS

Lithium hopping in $Nb_{12}WO_{33}$. Owing to the large unit cell and low symmetry (space group $C2$) of $Nb_{12}WO_{33}$, there are many inequivalent lithium positions. Each cavity contains multiple lithium positions, e.g. cavity II contains positions A, B, C, and D. These positions were previously described in Ref. [11], and are relabeled as compared to previous work for ease of presentation (Fig. 2a). Despite the fact that they are symmetrically inequivalent, they can be clustered based on their local structure. Fivefold coordinated 'pocket' sites (A, B, H, I) are found along the shear planes at the periphery of the block (red rectangle, Fig. 2). The other sites (C, D, E, F, G) are fourfold coordinated 'windows', described as 'horizontal' or 'vertical' depending on the orientation of the window relative to the plane of the block [11]. We note two subtleties about their local structure: (1) the

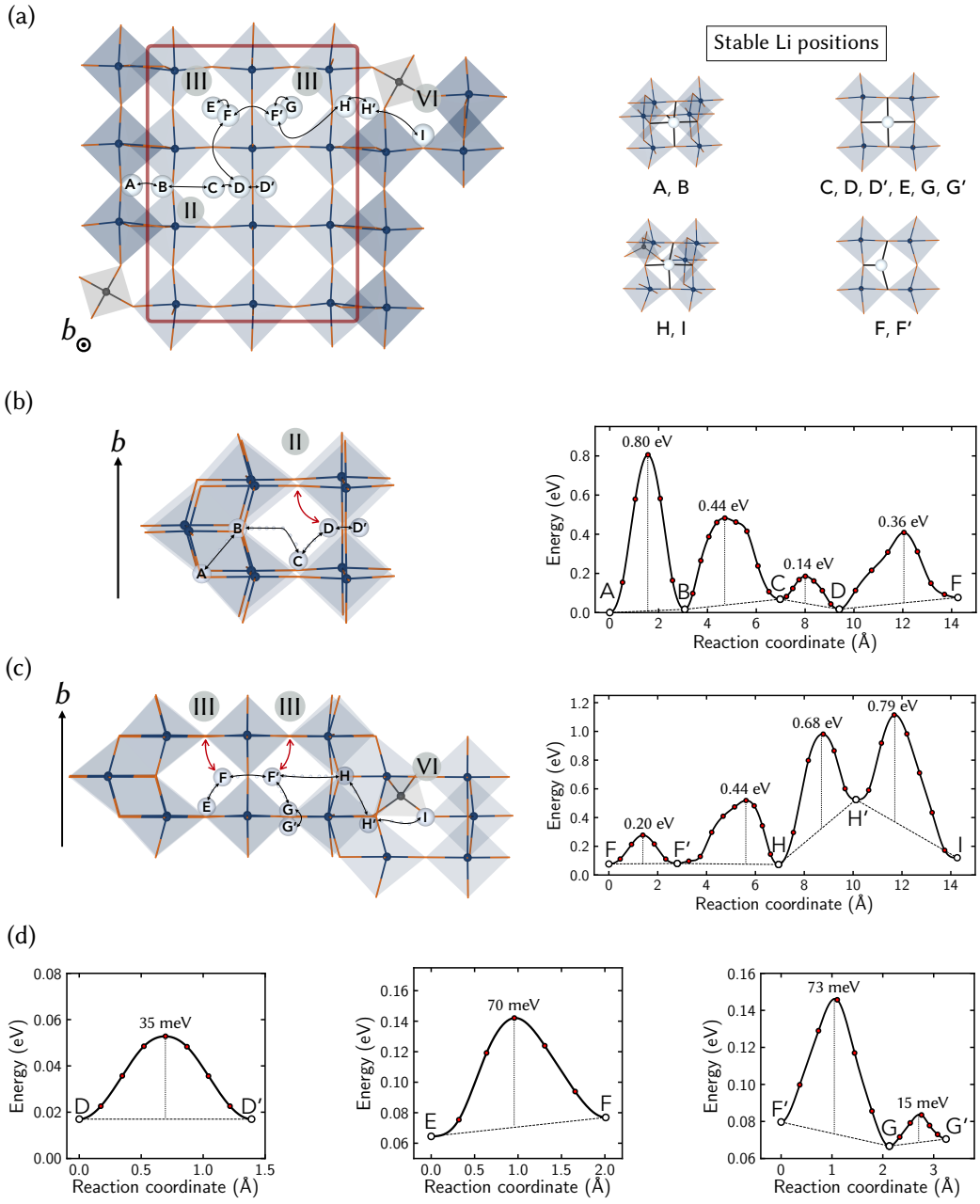

FIG. 2. Minimum energy paths and activation barriers (NEB) for lithium ion motion in $Nb_{12}WO_{33}$. (a) Lithium sites (A-I) and hops between them. A 3×4 block is framed by the red rectangle representing the shear planes. Cavities are labelled by type. (b) Hops and energy profiles/activation barriers in Cavity II and (c) Cavities III and VI. (d) Energy profile along the paths with very low barriers. Local rattling processes (D↔D', G↔G') show the lowest activation barriers (15–35 meV), followed by hops faciliating long-range diffusion down the *b* axis (C↔D, E↔F, G↔F', 70–140 meV). These *b*-axis hops percolate the structure through a chain of effectively equivalent jumps shown by the red arrows in (b) and (c). Cross-block motion (A↔B, H↔I) has very high activation barriers and is therefore slow. Niobium shown in dark blue, oxygen in orange, lithium in off-white, and tungsten in grey.

vertical window positions next to the shear planes (F, F') more strongly resemble threefold coordinated sites, and (2) in all window positions, the lithium ions sit above the plane formed by the oxygen atoms. A split position is present on the other side of the window. For example, Li ions in D and D' (Fig. 2a) are 0.5 Å above the plane formed by the four oxygens.

A continuous path (with a few branches) through the cavities in $Nb_{12}WO_{33}$ is shown in Fig. 2. This path does not include all possible barriers, even in the dilute limit, but rather all transitions between the different types of sites. Note that there is a twofold rotation axis running

through the center of the block, so that the unlabelled part is equivalent by symmetry. The two type III cavities in Fig. 2 are structurally very similar but not equivalent by symmetry, and are therefore both included in the path.

Results presented in Figure 2 show a clear hierarchy of activation barriers, and therefore lithium motion, in $Nb_{12}WO_{33}$. Very high barriers are found for motion from one block to another, either by crossing the shear plane (hop A↔B, $\Delta E_{\mathrm{KRA}} = 0.80$ eV, Fig. 2b), or by moving through cavity VI (H↔H'↔I, Fig. 2c) next to the tetrahedral site occupied by tungsten. The motion through cavity VI goes via a high energy intermediate H' site with an energy 0.6 eV above the most stable lithium site. The sequence of hops H↔H'↔I encounters a barrier of at least 1.0 eV. Due to the high activation barriers, lithium motion from one block to another in the *ac* plane will be very slow.

Hops from fivefold coordinated pocket sites at the block edges into the block center (B↔C, H↔F', Fig. 2b,c) present the next-largest barriers with values of 0.44 eV. This value is rather large compared to the barriers of other processes within the structure (see below). It suggests that hopping between the sites at the block edges and the sites in the block interior is slow, and the block-peripheral pocket sites are therefore somewhat isolated. The oxygen atoms that coordinate the lithium ions in the pocket sites are rigid because they belong to edges shared between octahedra. While moving out of the pocket site, the Li ion loses the local bonding interaction with the oxygens, which cannot bend towards the Li to support it. This leads to the relatively high activation barriers. The resulting minimum energy paths for B↔C and H↔F' hops involve Li almost 'floating' through the cavity (Fig. 2b,c). Note that there is no direct G↔H hop; an attempted NEB calculation for this hop goes via an intermediate F site.

Within the *ac* plane, Li can jump between cavities that belong to the same block with intermediate activation barriers (D↔F $E_a = 0.36$ eV, F↔F' $E_a = 0.2$ eV, Fig. 2b,c). Most of the hops within or out of cavity III are faciliated by the interstitial-like F and F' sites. As shown in Ref. [11] and by the AIMD simulations (see below), these F and F' sites disappear at higher lithium concentrations as the distortions of the framing octahedra are removed.

The most important hops are those that facilitate long-range diffusion along the *b* axis, specifically C↔D in cavity II, and E↔F and F'↔G in cavities III. These processes have low barriers of 70–140 meV, and cover jump distances of 1.9 Å, half the *b* lattice parameter. Note that these hops form percolating chains along the *b* axis, shown by the red arrows in Fig. 2b,c.

In addition, there are processes with ultra-low barriers that are associated with 'rattling' in the fourfold coordinated window positions (D↔D', G↔G'). As described above, the Li ion sits slightly above the plane formed by the four coordinating oxygen atoms of the window. An equivalent position is found on the other side of the plane. Barriers for these local rattling processes are in the range of 15–35 meV, on the order of the thermal energy at room temperature ($k_BT = 25$ meV). For these ultra-low barrier processes, the coordination of the Li ion barely changes during the motion, explaining the very low activation energies. The transition states are also fourfold coordinated Li ions, sitting within the window formed by the framing oxygen atoms, rather than slightly above or below. Due to the low barriers and small distances, it is more accurate to describe this motion as an anharmonic vibration, rather than a Li ion jump.

Lithium hopping in $Nb_{14}W_3O_{44}$. The 4×4 blocks of $Nb_{14}W_3O_{44}$ feature a type I cavity in the middle of the block, which is not present in $Nb_{12}WO_{33}$. In our structure model, tungsten occupies the tetrahedral site and two of the block-central transition metal sites (Fig. 3). The parent structure has a fourfold rotation axis through the middle of the block. Note that $Nb_{14}W_3O_{44}$ has a different axis system than $Nb_{12}WO_{33}$; the blocks lie in the *ac* plane in $Nb_{12}WO_{33}$, but in the *ab* plane in $Nb_{14}W_3O_{44}$, due to the different space group.

The lithium diffusion paths and associated activation barriers for $Nb_{12}WO_{33}$ and $Nb_{14}W_3O_{44}$ are very similar: the barrier for crossing from one block to another through the crystallographic shear plane is again very high (A↔B, $\Delta E_{\mathrm{KRA}} = 0.82$ eV). The hop from the pocket site at the edge of the block to a window site (B↔C) has the next-largest activation barrier of 0.42 eV.

The cross-cavity motion from type II to III has a high barrier (D↔F, 0.28 eV) compared to the II to I motion (C↔D↔D'↔G, max. barrier 0.11 eV). The D→F hop takes place next to octahedra at the shear plane, which share edges and are strongly distorted. The octahedra framing the path from cavity II to I on the other hand are exclusively corner-sharing and do not show these strong distortions. One of the oxygen atoms of the window next to the shear plane is part of a shared edge, therefore less flexible and less effective at supporting the Li ion during the D↔F hop, which leads to the higher activation barrier. This rigidity of the oxygen atoms that are part of shared edges between octahedra is also responsible for the absence of stable lithium positions within the distorted windows (cf. F sites), and the high barrier for hops between pocket sites and the block interior (see above). A similar pattern is also found in $Nb_{12}WO_{33}$ (Fig. 2), where the motion between the type II cavities through the central window shows a much lower activation barrier than the hops next to the shear planes. AIMD simulations (see below) confirm this pattern.

Cavities of type I are approximately cubic and show the least distorted octahedra in the structure (Fig. 3a,b). Li motion within cavity I is facile with low activation barriers for hopping between the window sites (80 meV, Fig. 3b), and even lower barriers for the rattling process within window sites (e.g. G↔G', 30 meV). Cavity I is connected to four type II cavities via low barrier hops, which suggests that it facilitates Li motion within the

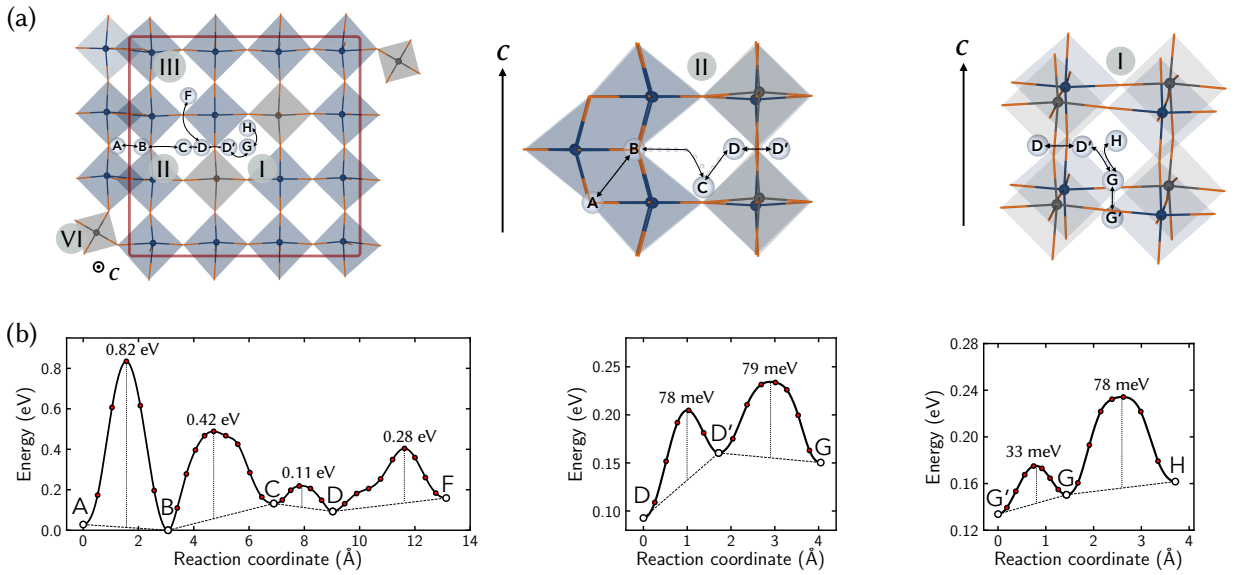

FIG. 3. Minimum energy paths and activation barriers (NEB) for lithium ion motion in $Nb_{14}W_3O_{44}$. (a) View of the hopping pathways within the block and within individual cavities. (b) Activation barriers for lithium motion. Barriers are especially low for motion within cavity I. Long-range diffusion occurs almost exclusively along the c axis, but Li ion motion in the ab plane is possible within a single block (red rectangle). Niobium shown in dark blue, oxygen in orange, lithium in off-white, and tungsten in grey.

block plane to a much greater extent than the cavities next to the shear planes.

The lowest energy barriers are found for motion along the c axis in $Nb_{14}W_3O_{44}$ (C↔D in cavity II, G↔D', G↔H in cavity I), with values between 80–110 meV. These hops can occur in Cavities I, II and III, even though hops within III were not explicitly calculated for $Nb_{14}W_3O_{44}$. The dominant diffusion pathway will therefore be along the c axis (cf. b axis in $Nb_{12}WO_{33}$).

There are a number of subtleties regarding the interpretation of the NEB results for both $Nb_{12}WO_{33}$ and $Nb_{14}W_3O_{44}$ that are worth mentioning. The barriers are reported as kinetically resolved barriers (cf. Methods) to remove the direction dependence for hops that have endpoints with different energies. In terms of the activation barrier for diffusion, it is the larger of the two barriers that will be relevant (e.g. the D→C hop has a larger barrier than C→D for $Nb_{12}WO_{33}$, Fig. 2). Another point to note is that not all lithium sites have the same energy, and the first lithium ions that are inserted into the structure will predominantly occupy the lower energy pocket sites at the block edges. However, the other lithium sites in the block interior are well within an accessible energy range of less than 100 meV for $Nb_{12}WO_{33}$, and are entropically favoured due to the fact that the potential energy landscape is inherently flatter in the block interior than at the block edges, resulting in softer vibrational modes. Furthermore, lithium ions in the lower energy sites do not inhibit transport as they are tucked away in pockets at the block periphery. For $Nb_{14}W_3O_{44}$, there is the additional complication of appreciable Nb/W cation disorder, which will modify both the site energies and activation barriers for lithium motion. All of these considerations suggest that even at very dilute lithium concentrations, there is a population of lithium ions within the block interior that can diffuse with activation barriers of 0.1–0.2 eV.

Li Probability Density. AIMD simulations were performed to study the lithium dynamics explicitly at a range of lithium concentrations. Isosurfaces of the lithium ion probability density of $Li_5Nb_{12}WO_{33}$ are shown in Fig. 4. The lithium probability density $P(\mathbf{r})$ is related to an effective free energy landscape for lithium ions, $E(\mathbf{r})$, via $P(\mathbf{r}) \propto e^{-\frac{E(\mathbf{r})}{k_B T}}$. Stable sites (purple isosurface in Fig. 4) are in agreement with those seen in the NEB calculations (side-by-side comparison of NEB and AIMD in Fig. S5). The dominant diffusion paths run along the b axis in one-dimensional channels within each cavity (light blue isosurface in Fig. 4). Interestingly, the movement in the ac plane is dominated by hops between the two type II cavities in the center, which are connected by a bridge. Movement between the remaining diffusion channels in type III cavities, and hops between the five-fold coordinated sites and the 1D channels, is much less probable. This is consistent with the results obtained from nudged elastic band calculations: hops through the windows next to the shear planes, and hops between five-fold coordinated sites and those in the block centre, have much higher activation energies than the movement down the tunnels, or the rattling within the central window.

The Li probability density isosurface for $Li_8Nb_{14}W_3O_{44}$ (Fig. S7) shows the same patterns: a connected diffusion network between cavities of type I

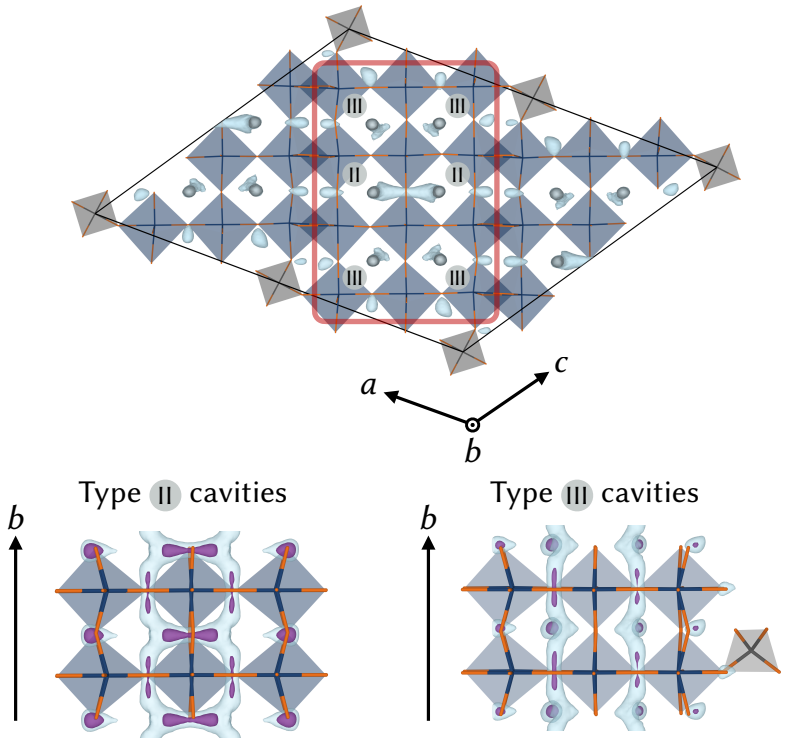

FIG. 4. Li-ion probability density distribution within $Li_5Nb_{12}WO_{33}$ obtained from AIMD simulations. Views parallel to the b axis (top) and perpendicular to the b axis (bottom). Isosurface values are $P = P_{max}/30$ (light blue) and $P = P_{max}/5$ (purple). The network of connected sites participating in diffusion along the b axis is restricted to the block interior. While the tunnels in cavities II (bottom left) are connected to each other via a bridge, the tunnels in cavities of type III (bottom right) are isolated. Diffusion channels and stable lithium sites are in very good agreement with NEB results (cf. Fig. 2b,c and Fig. S5).

and II, which is not connected to channels in cavities III. $Li_8Nb_{12}WO_{33}$ and $Li_8Nb_{14}W_3O_{44}$ share these patterns due to the fact that cavities of the same type are structurally very similar, even if they are found in blocks of different sizes.

At higher lithium concentrations, the transition metal–oxygen framework of the structure changes; distortions of octahedra next to the crystallographic shear planes are removed and the window sites next to the shear planes become stable sites for lithium occupation. This is linked to a contraction of the lattice parameters in the block plane [11]. The structural change is a function of lithium concentration, and is not present in $Li_5Nb_{12}WO_{33}$, partly in $Li_8Nb_{12}WO_{33}$ (Fig. S6), and fully in $Li_{17}Nb_{12}WO_{33}$. Stable lithium positions appear in the previously unstable distorted window sites, forming bridges between type III cavities in $Li_8Nb_{12}WO_{33}$ (Fig. S7). The diffusion remains one-dimensional within tunnels running along the b axis.

AIMD - Quantitative Analysis. Various problems were encountered during the AIMD simulations. The temperatures of AIMD simulations have to be high enough to see lithium motion on the timescale that is accessible, but above 900 K defect formation was observed in the host structure (see below). This limited the available temperature range to 600–900 K. In terms of the stoichiometries, a large number of lithium ions are required for sufficient statistics. However, if the concentration of Li ions is too large, the dynamics becomes very sluggish. These problems led to only two stoichiometries ($Li_8Nb_{12}WO_{33}$ and $Li_8Nb_{14}W_3O_{44}$) having enough data to do a quantitative analysis of the diffusion coefficients. The analysis of the lithium probability density distributions above was performed for AIMD simulations at a single temperature, for which sufficient data was available for all stoichiometries.

Stoichiometry	Li/TM	$D^{\perp,*}_{298K}$ (m^2s^{-1})	E_a (eV)
$Li_8Nb_{12}WO_{33}$	0.615	$1.8 \cdot 10^{-12}$	0.31 ± 0.05
$Li_8Nb_{14}W_3O_{44}$	0.471	$3.2 \cdot 10^{-11}$	0.23 ± 0.03

TABLE I. Diffusion coefficients and activation energies obtained from AIMD simulations. The diffusion is highly anisotropic and only the value along the direction perpendicular to the block plane $D^{\perp}$ is reported (b axis in $Nb_{12}WO_{33}$, c axis in $Nb_{14}W_3O_{44}$).

The diffusion coefficients over the temperature range 600–900 K for $Li_8Nb_{12}WO_{33}$ and $Li_8Nb_{14}W_3O_{44}$ are plotted in Fig. 5 together with an Arrhenius fit. The resulting room temperature diffusion coefficients and activation energies are listed in Table I. The diffusion coeffi-

cients are extracted by fitting the component of the MSD perpendicular to the block plane, which corresponds to the b axis in $Nb_{12}WO_{33}$, and to the c axis in $Nb_{14}W_3O_{44}$. The diffusion coefficients are denoted $D^{\perp}$ to make this clear. The MSD within the block plane is not even linear due to the hard boundary formed by the shear planes. $Li_8Nb_{14}W_3O_{44}$ shows faster diffusion than $Li_8Nb_{12}WO_{33}$ and the data for this compound is a better fit to the Arrhenius expression, with a lower error on the estimate of the activation energy.

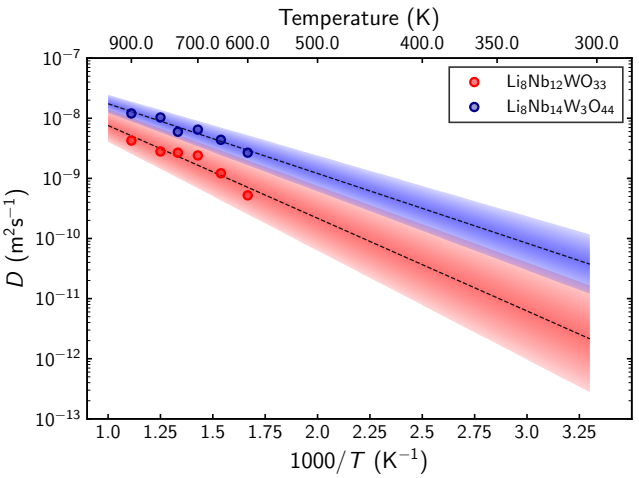

FIG. 5. Arrhenius plot of AIMD simulation results for $Li_8Nb_{12}WO_{33}$ (red) and $Li_8Nb_{14}W_3O_{44}$ (blue). The shaded region corresponds to extrapolation including standard errors of the activation energies.

The activation energies for $Li_8Nb_{12}WO_{33}$ and $Li_8Nb_{14}W_3O_{44}$ are between 0.2–0.3 eV, slightly larger than those obtained from NEB results (0.1–0.2 eV). The increase in the activation energy is attributed to the much larger lithium concentrations that are probed in the AIMD simulations (roughly 0.5 Li/TM), which result in repulsive Li–Li interactions, increasing the activation energies for Li-ion hops. The extrapolated room temperature diffusion coefficients are high (10^{-12}–10^{-11} m^2s^{-1}), comparable with values for solid electrolytes [6, 25]. The activation barrier is lower, and the diffusion coefficient higher, for $Li_8Nb_{14}W_3O_{44}$ than for $Li_8Nb_{12}WO_{33}$. Both the lower lithium content and the structural framework with more and better connected tunnels are likely responsible for this.

Tungsten interstitial defects. For AIMD simulations above 900 K, tetrahedrally coordinated tungsten atoms within the type VI cavities were observed to migrate into adjacent octahedral positions (Fig. 6). These interstitial defects were observed for both $Li_8Nb_{12}WO_{33}$ and $Li_{17}Nb_{12}WO_{33}$, and occurred more frequently with increasing temperature and lithium content. This indicates that the activation barrier for the migration of tungsten decreases with increasing lithium concentration. The decrease in the activation barrier might be due to the reduction of the transition metal ions and the removal of distortions within transition metal–oxygen octahedra, both of which are known to occur as the lithium concentration increases [6, 11]. Activation barriers for this tungsten migration can not be obtained directly from the AIMD simulations. However, given that the formation of the defects occurred only above 900 K, and Li-ions are already observed to be mobile below that temperature, we can conclude that the tungsten migration barrier is significantly larger than that for Li-ion migration. Meaningful lithium diffusion coefficients were not extracted from simulations exhibiting these defects because the host framework had changed, with new lithium positions and diffusion pathways within the type VI cavities. This limited the temperature range for AIMD simulations to 600–900 K. We note that this type of tungsten interstitial defect was previously observed experimentally, and was suggested to explain off-stoichiometry in block-type niobium oxide structures [26]. It could also be present in small concentrations in the niobium tungsten oxides after synthesis. A detailed investigation of these defects is left to future work.

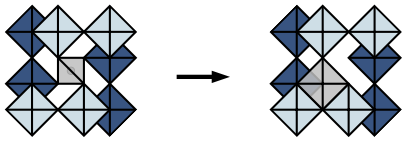

FIG. 6. Interstitial defect observed to form in type VI cavities by migration of tungsten from a tetrahedral site into an adjacent octahedral site.

IV. DISCUSSION

Overall, the diffusion mechanism in niobium tungsten oxides with crystallographic shear structures is strongly anisotropic, effectively one-dimensional down the tunnels, in agreement with previous suggestions [6, 14, 15]. Hops within the block plane are facile but eventually hit the boundaries presented by the shear planes, which prevent long-range motion perpendicular to the tunnels. The Li-ion dynamics within the structures is constrained to occur within blocks. NEB calculations show activation barriers of 0.1–0.2 eV in the dilute limit, and AIMD simulations suggest activation barriers of 0.2–0.3 eV at concentrations around 0.5 Li/TM. At those concentrations, AIMD simulations predict room temperature diffusion coefficients in the range of 10^{-12}–10^{-11} m^2s^{-1}, on par with the best known solid electrolytes.

In addition to the overall mechanism, a number of structure-specific details are worth discussing. The diffusion of lithium ions in the structure occurs mostly through hops between fourfold coordinated window sites, which are located in the block interior. Hops into or out of fivefold coordinated pocket sites occur much less fre-

quently, because these hops have large activation barriers. The pocket sites are also connected to fewer neighbouring Li positions than the window sites. If the parallel 1D diffusion channels are a 'multi-lane highway' [6], the pocket sites are essentially parking spots.

We can expand on the role of the pocket sites at the block edges a little more: at dilute lithium concentrations, there is a question as to whether lithium ions are trapped in those sites or not. There is a notable asymmetry between lithium intercalation and deintercalation here: starting with an empty Nb/W oxide structure, the lithium ions have to enter the structure through one of the channels, which will be exposed at surfaces of the particles. In contrast, there is no direct way to enter one of the pocket sites.

Once in the channels, ions are much more likely to diffuse down the channels than move into the fivefold coordinated pocket sites, due to the difference in the activation energies. The relative probability can be estimated by the ratio of the rates. Assuming activation energies of 0.14 eV for down-tunnel motion (cf. Fig. 2, C↔D), 0.44 eV for a transition into a pocket site (cf. Fig. 2, B↔C), and a rate expression $\Gamma \propto e^{-\frac{E_a}{k_B T}}$, the down-tunnel motion is faster by a factor of

$$\frac{\Gamma_{\mathrm{in-tunnel}}}{\Gamma_{\mathrm{tunnel\to pocket}}} = \frac{e^{-0.14\mathrm{eV}/k_B T}}{e^{-0.44\mathrm{eV}/k_B T}} \approx 1.6 \cdot 10^5$$

for $T = 293$ K. Hence, once an ion is in the channel, down-tunnel transport is overwhelmingly likely, and lithium ions therefore move down the tunnels rapidly before finally making a transition into a pocket site. Now consider the reverse process of deintercalation: to pull lithium ions in pocket sites out, they first have to make a transition into the channels. But this is a slow process, and lithium ions in the pocket sites could remain trapped during high-rate deintercalation. Based on these considerations, and the fact that there will likely be partial occupation of many sites at low lithium concentrations (cf. Results), the pocket sites only significantly inhibit fast lithium ion motion during high-rate deintercalation. The practical implication for full battery cells with niobium tungsten oxide anodes is that the charging process may be faster than discharge, which is compatible with most applications such as regenerative braking, fast charging electronics, and others, that can utilize high input power densities.

The different types of cavities contain different stable lithium positions and diffusion channels, but these are remarkably transferable between different compounds (i.e. $Nb_{12}WO_{33}$ and $Nb_{14}W_3O_{44}$). Most notably, the type III cavities at the block corners present more isolated diffusion channels compared to the type I and II cavities. As mentioned previously, this is due to the fact that motion from a type III cavity into any neighbouring cavity in the block plane must proceed via a distorted window, which does not feature a stable intermediate lithium position. On the other hand, moving out of type I or II cavities through an undistorted window is easier due to an intermediate stable Li position and hence a lower overall activation energy. Given the cross-compound transferability of the properties of the different cavity types, one can easily extrapolate what the lithium motion will look like in shear structures $Nb_{16}W_5O_{55}$ and $Nb_{18}W_8O_{69}$, even though they were not studied explicitly in this work. Overall, the shear structures of niobium tungsten oxides present a complex energy landscape for lithium motion, with very different barrier sizes: a flat landscape in the interior giving rise to fast lithium diffusion, high barriers for pocket sites, and very high barriers for moving between blocks.

Due to these differences between cavity types, it seems that structures with the maximum number of type I and II cavities show the most interconnected diffusion network and the fastest lithium diffusion. These would also be the structures with the largest block sizes. Considering the four known niobium tungsten oxide single block structures ($Nb_{12}WO_{33}$, $Nb_{14}W_3O_{44}$, $Nb_{16}W_5O_{55}$, and $Nb_{18}W_8O_{69}$), it is therefore likely that the diffusion is fastest in $Nb_{18}W_8O_{69}$, although it is questionable whether these differences can be accurately measured. Of course, this argument is based on structural considerations and neglects the impact of a changing ratio between niobium and tungsten. The niobium tungsten oxides are also partially disordered [11, 27], and while we have not explored the effect of the cation disorder on the diffusion, it could be important.

True one-dimensional diffusion is special because the diffusing particles cannot pass each other. In fact, the tracer diffusion coefficient for pure 1D diffusion is zero, due to the fact that the mean-square displacement grows as the square root of the time, rather than linearly [28]. In the niobium tungsten oxides, jumps between the one-dimensional channels are therefore required to obtain a non-zero tracer diffusion coefficient. It would be interesting to examine to what extent the constrained, effectively one-dimensional ionic motion is correlated, especially within the more isolated tunnels at the block corners. We stress that this applies only to *tracer* diffusion, not to *chemical* diffusion in 1D, which is still well defined. The tracer diffusion coefficient describes motion of a single (tagged) particle, whereas the chemical diffusion coefficient is related to collective (mass) transport [22, 28]. While the transport coefficient is relevant for rate performance, it is the tracer diffusion coefficient that has been measured by pulsed-field-gradient (PFG) NMR spectroscopy measurements on lithiated niobium tungsten oxide phases. The PFG NMR experiments should therefore be sensitive to the correlation effects, especially in shear phases with smaller blocks.

The PFG NMR measurements on $Li_xNb_{16}W_5O_{55}$ show room temperature diffusivities of 10^{-13}–10^{-12} m^2s^{-1} and activation energies of 0.1–0.2 eV [6], while $Li_xNb_{18}W_8O_{69}$ shows even higher diffusivities of 10^{-12}–10^{-10} m^2s^{-1} [14]. These measurements were performed for lithium concentrations up to 0.4 Li/TM, and probe

long-range lithium transport. Measurements on the two phases studied in this work, $Nb_{12}WO_{33}$ and $Nb_{14}W_3O_{44}$, are not currently available. However, given the cross-compound transferability demonstrated in this work, we can tentatively compare values: both activation energies and the magnitude of the diffusion coefficients are comparable, although lithium concentrations in this work are either much lower (NEB) or higher (AIMD) than in the experiments. The results presented in this work place the experimentally derived values into context and offer a detailed structural understanding of the mechanism. PFG NMR experiments only measure long-range lithium motion that contributes to diffusion. NMR relaxometry experiments, on the other hand, probe all types of lithium motion (including local motion) and provide estimates of barriers. Relaxometry experiments would therefore be very useful to understand the hopping motion and associated barriers in more detail. It is unfortunate that the high computational cost of AIMD simulations prevents a more detailed study of the diffusion coefficients and activation barriers as a function of concentration at this time. Classical MD studies with appropriate potentials would be very useful as an avenue for future work in this direction.

V. CONCLUSION

In this work, we have used density-functional theory calculations to study the lithium diffusion in niobium tungsten oxide shear structures. Lithium diffusion takes place in parallel tunnels, but is constrained to be effectively one-dimensional by the crystallographic shear planes. The Li-ion jumps that contribute to long-range diffusion have activation energies of 0.1–0.2 eV in the dilute limit, and slightly larger barriers at higher lithium concentrations (around 0.5 Li/TM). The low activation barriers lead to high room temperature diffusivities (10^{-12}–10^{-11} m^2s^{-1} for stoichiometries probed in this work), and are responsible for the excellent high-rate capability of the niobium tungsten oxides in lithium ion batteries.

While the Li-ion motion that contributes to long range diffusion takes place by jumps between window sites in the block interior, there are a number of other processes occuring within the structure: local rattling motions, and jumps between window and pocket sites. In addition, the lithium motion is different depending on the cavity type. The activation barriers for jumps between different types of sites are transferable between different niobium tungsten oxides, due to their strong structural similarity. Overall, these results paint a clear picture of the diffusion mechanism in niobium tungsten oxide shear structures, and illustrate the relationship between the diffusion mechanism and the atomic structure of the materials. The same relationships should hold in other crystallographic shear phases as well.

ACKNOWLEDGMENTS

C.P.K. thanks Dr Bora Karasulu for useful discussions and advice regarding *ab initio* molecular dynamics simulations. We acknowledge the use of Athena at HPC Midlands+, which was funded by the EPSRC on grant EP/P020232/1, in this research via the EPSRC RAP call of spring 2019. This work also used resources provided by the Cambridge Service for Data Driven Discovery (CSD3) operated by the University of Cambridge Research Computing Service, funded by the EPSRC (EP/P020259/1), and DiRAC funding from the STFC. C.P.K. thanks the Winton Programme for the Physics of Sustainability and EPSRC for financial support. K.J.G. thanks the Winston Churchill Foundation of the United States and the Herchel Smith Foundation. K.J.G. and C.P.G. also thank the EPSRC for funding under a program grant (EP/M009521/1). C.P.G. thanks the EU ERC for an advanced fellowship (EC H2020 835073).

Supporting Information. Further computational details including supercell construction, parameter validation for AIMD simulations, Li-ion probability density plots for $Li_8Nb_{14}W_3O_{44}$, $Li_8Nb_{12}WO_{33}$, and $Li_{17}Nb_{12}WO_{33}$. Data supporting this work are available at www.repository.cam.ac.uk.

[1] Y. Liu, Y. Zhu, and Y. Cui, Nature Energy **4**, 540 (2019).
[2] A. Lennon, Y. Jiang, C. Hall, D. Lau, N. Song, P. Burr, C. P. Grey, and K. J. Griffith, MRS Energy & Sustainability **6**, E2 (2019).
[3] R. J. Cava, D. W. Murphy, and S. M. Zahurak, Journal of The Electrochemical Society **130**, 2345 (1983).
[4] K. J. Griffith, A. C. Forse, J. M. Griffin, and C. P. Grey, Journal of the American Chemical Society **138**, 8888 (2016).
[5] N. Takami, K. Ise, Y. Harada, T. Iwasaki, T. Kishi, and K. Hoshina, Journal of Power Sources **396**, 429 (2018).
[6] K. J. Griffith, K. M. Wiaderek, G. Cibin, L. E. Marbella, and C. P. Grey, Nature **559**, 556 (2018).
[7] D. Saritha, V. Pralong, U. V. Varadaraju, and B. Raveau, Journal of Solid State Chemistry **183**, 988 (2010).
[8] L. Yan, H. Lan, H. Yu, S. Qian, X. Cheng, N. Long, R. Zhang, M. Shui, and J. Shu, Journal of Materials Chemistry A **5**, 8972 (2017).
[9] A. F. Fuentes, E. B. Garza, A. M. de la Cruz, and L. M. Torres-Martínez, Solid state ionics **93**, 245 (1997).
[10] L. Yan, J. Shu, C. Li, X. Cheng, H. Zhu, H. Yu, C. Zhang, Y. Zheng, Y. Xie, and Z. Guo, Energy Storage Materials **16**, 535 (2019).
[11] C. P. Koçer, K. J. Griffith, C. P. Grey, and A. J. Morris, Journal of the American Chemical Society **141**, 15121

(2019).
[12] R. J. Cava, B. Batlogg, J. J. Krajewski, H. F. Poulsen, P. Gammel, W. F. Peck, and L. W. Rupp, Physical Review B **44**, 6973 (1991).
[13] C. P. Koçer, K. J. Griffith, C. P. Grey, and A. J. Morris, Physical Review B **99**, 075151 (2019).
[14] K. Griffith and C. Grey, (2019), 10.26434/chemrxiv.11231153.v1.
[15] K. J. Griffith, I. D. Seymour, M. A. Hope, M. M. Butala, L. K. Lamontagne, M. B. Preefer, C. P. Koçer, G. Henkelman, A. J. Morris, M. J. Cliffe, S. E. Dutton, and C. P. Grey, Journal of the American Chemical Society **141**, 16706 (2019).
[16] G. Henkelman, B. P. Uberuaga, and H. Jónsson, The Journal of Chemical Physics **113**, 9901 (2000).
[17] G. Kresse and J. Furthmüller, Physical Review B **54**, 11169 (1996).
[18] P. E. Blöchl, Physical Review B **50**, 17953 (1994).
[19] J. P. Perdew, A. Ruzsinszky, G. I. Csonka, O. A. Vydrov, G. E. Scuseria, L. A. Constantin, X. Zhou, and K. Burke, Physical Review Letters **100**, 136406 (2008).
[20] A. Van der Ven, G. Ceder, M. Asta, and P. D. Tepesch, Physical Review B **64** (2001), 10.1103/PhysRevB.64.184307.
[21] A. Urban, D.-H. Seo, and G. Ceder, npj Computational Materials **2**, npjcompumats20162 (2016).
[22] A. Van der Ven, Z. Deng, S. Banerjee, and S. P. Ong, Chemical Reviews (2020), 10.1021/acs.chemrev.9b00601.
[23] Z. Zhu, I.-H. Chu, Z. Deng, and S. P. Ong, Chemistry of Materials **27**, 8318 (2015).
[24] K. Momma and F. Izumi, Journal of Applied Crystallography **44**, 1272 (2011).
[25] J. C. Bachman, S. Muy, A. Grimaud, H.-H. Chang, N. Pour, S. F. Lux, O. Paschos, F. Maglia, S. Lupart, P. Lamp, L. Giordano, and Y. Shao-Horn, Chemical Reviews **116**, 140 (2016).
[26] J. S. Anderson, J. M. Browne, A. K. Cheetham, R. V. Dreele, J. L. Hutchison, F. J. Lincoln, D. J. M. Bevan, and J. Straehle, Nature **243**, 81 (1973).
[27] A. K. Cheetham and N. C. Allen, Journal of the Chemical Society, Chemical Communications **0**, 1370 (1983).
[28] P. Heitjans and J. Kärger, eds., Diffusion in Condensed Matter (Springer-Verlag, Berlin/Heidelberg, 2005).